

Performance Evaluation of Printable Carbon-Based Perovskite Solar Cells Infiltrated with Reusable CsPbI_3 : EuCl_3 and Standard AVA-MAPbI₃

Salvatore Valastro, Gaetano Calogero, Emanuele Smecca, Corrado Bongiorno, Valentina Arena, Giovanni Mannino, Ioannis Deretzis, Giuseppe Fisicaro, Antonino La Magna, and Alessandra Alberti*

Hole-transporting layer-free mesoporous carbon (mC) architectures represent a printable, low-cost, and stable solution for the future commercialization of perovskite solar cells (PSCs). CsPbI_3 perovskite is attracting attention for its inorganic structure, which yields higher structural stability compared to hybrid counterparts and allows reversibility of its photoactive phase. Here the photovoltaic performance of large-area (144 mm^2) devices infiltrated with CsPbI_3 : EuCl_3 is systematically evaluated, using AVA-MAPbI₃ mC-PSCs as a reference.

Measured and simulated J - V curves acquired at various scan rates show a significantly reduced hysteresis for Eu-doped CsPbI_3 with respect to AVA-MAPbI₃ mC-PSCs. The synergic comparison between experiments and simulations reveals the complex interplay between ionic and electronic charges in the two mC-PSCs, supporting the argument that cation migration is suppressed in CsPbI_3 : EuCl_3 . This also agrees with steady-state photoconversion efficiency measured and simulated at fixed bias, which is constant over time in CsPbI_3 : EuCl_3 , contrary to what occurs in AVA-MAPbI₃ where a decay arises from enhanced ionic migration. In addition, CsPbI_3 : EuCl_3 mC-PSCs maintain their initial efficiency up to 250 h at 55 °C under continuous illumination during maximum power point tracking measurements. The possibility of reusing the CsPbI_3 : EuCl_3 mC-PSCs multiple times is demonstrated, pointing out the superiority of this inorganic perovskite in terms of sustainability.

1. Introduction


Perovskite solar cells (PSC) have great potential in the photovoltaic (PV) field due to their peculiar optoelectronic properties,^[1] which allow reaching a certified photoconversion efficiency of 26.1%^[2,3] as in silicon solar cells. Promising use of this technology is tandem perovskite/silicon solar cells, recently reaching the record efficiency of 33.9%^[3,4] and indoor use of PSCs for Internet of Things^[5] by exploiting the favorable perovskite (PSK) bandgap. Although for some applications semitransparent PSCs are mandatory, for some others opaque devices are applicable.

Despite the high efficiency reached in the last years, the route toward commercialization of PSK-based photovoltaic technologies is still challenging. One concern is the presence of lead in the perovskite formulation that, in contrast, enables the high efficiency.^[6,7] The main technological issues rely on the up-scalability of the technology, with the efficiency record achieved on small-area devices ($<0.1 \text{ cm}^2$), and on the device performance instability.^[8] The first

is related to the deposition methods traditionally used in the PSCs layer fabrication (e.g., spin-coating) which do not allow the production of uniform layers on large-area, resulting in lower efficiency.^[9] The second depends on the sensitivity of the perovskite to external factors like moisture,^[10] UV,^[11] temperature,^[12] and on the interfaces with the charge transporting layers (CTLs).^[13] In addition, metal top electrode (Au, Ag, and Al)^[14,15] can diffuse through the CTL (e.g., Spiro-OMeTAD)^[16] into the perovskite layer, thus affecting the durability of PSCs.

Among the device architectures, mesoporous carbon (mC) hole transporting layer (HTL)-free mesoporous carbon PSC (mC-PSC) are promising since they are 1) printable, allowing uniform large-area deposition, 2) low-cost, not using expensive organic HTL and the metallic top electrode,^[17] and 3) stable, because the carbon electrode, differently from traditional organic transporting layer or metallic top electrodes, does not react with halides of the perovskite.^[18,19] The architecture consists of a

S. Valastro, G. Calogero, E. Smecca, C. Bongiorno, V. Arena, G. Mannino, I. Deretzis, G. Fisicaro, A. La Magna, A. Alberti
Institute for Microelectronics and Microsystems (IMM)
National Research Council (CNR)
Zona Industriale Strada VIII n.5, Catania 95121, Italy
E-mail: alessandra.alberti@imm.cnr.it

 The ORCID identification number(s) for the author(s) of this article can be found under <https://doi.org/10.1002/solr.202300944>.

© 2024 The Authors. Solar RRL published by Wiley-VCH GmbH. This is an open access article under the terms of the Creative Commons Attribution-NonCommercial License, which permits use, distribution and reproduction in any medium, provided the original work is properly cited and is not used for commercial purposes.

DOI: 10.1002/solr.202300944

triple mesoporous (mp) stack of mp-TiO₂/mp-ZrO₂/mp-carbon on Glass/FTO/compact-TiO₂ substrate.^[20] The ZrO₂ layer works as an insulating layer to avoid contact between carbon and TiO₂. The perovskite precursor solution can be infiltrated into the mesoporous stack by different methods like semi-automatic dispensing system or ink-jet printing.^[21] The last two methods guarantee a better layer uniformity than manual drop-casting, and thus higher efficiency on large-area devices.^[22]

Different composition of perovskite was used in mC-PSCs. The most used in the literature is the (5-AVA)_xMA_{1-x}PbI₃ (AVA-MAPbI₃)^[23] perovskite that is stable, surpassing the IEC61215:2016 Standards and resistant to reverse bias induced degradation.^[24] The AVA-MAPbI₃ mC-PSC has reached the record efficiency of 14% in a small-area device (9 mm²) through an additional humidity thermal treatment on the device, specifically 40 °C with 75% RH for 150 h.^[25] Large area devices are in some cases explored but with a loss of the yield as further discussed along the article. Another perovskite recently integrated into the mesoporous stack is Rb_{0.05}Cs_{0.1}FA_{0.85}PbI₃^[26] a triplecation perovskite that has shown a certified efficiency of 15.5% in a small-area device (9 mm²), with a high fill factor (FF) of 78.8%. In our previous work,^[27] we proposed the europium-doped CsPbI₃ formulation of perovskite to be infiltrated into mC-PSCs. The main doping effect is that a γ -phase is formed at low temperatures (80–90 °C) and it is retained much longer than in undoped CsPbI₃.^[27,28] Moreover, defect states populate the intra-gap region if Eu is not added, with effects on the device performances.^[27] We have shown that the PSCs can reach an efficiency of 9.2% in a small-area device (4.2 mm²), a value much higher than the one exhibited by pure CsPbI₃ (2%). Moreover, the meso-devices with europium-doped CsPbI₃, differently from mC-PSC with AVA-MAPbI₃, can be reused by exploiting the reversibility from δ -yellow to γ -black phase that occurs at 350 °C. The reuse of mC-PSC has been shown,^[27] enabled by the temperature-resistant stack without HTL and metals.

In this article, we present a comparative study of mC-PSCs infiltrated with CsPbI₃:EuCl₃ and reference AVA-MAPbI₃ by manual drop-casting method. We focus on the photovoltaic performances of 144 mm² devices which are more representative of the average behavior compared to the small-area devices. Scan speed of J - V measurements and related ionic migration is deeply investigated and put in relationship with the different behavior of MA⁺ and Cs⁺ cations. Device simulations provide deep insights into the device's working mechanism, explaining the different photovoltaic behavior of the CsPbI₃:EuCl₃ mC-PSCs compared to the reference AVA-MAPbI₃ mC-PSCs. The reusability of CsPbI₃:EuCl₃ mC-PSC in the light of sustainability is investigated, prospecting possible routes to improve it further.

2. Results and Discussion

We infiltrated two different perovskite precursor solutions, CsPbI₃:EuCl₃ and AVA-MAPbI₃, which is used as a reference, into mC-PSCs through a manual drop-casting method. The Glass/FTO/c-TiO₂/mp-TiO₂/mp-ZrO₂/mp-Carbon stack and the AVA-MAPbI₃ precursor solution are commercially available (Solaronix) while the CsPbI₃:EuCl₃ precursor solution is prepared as in ref. [29,30] and reported in the Supporting

Information. The AVA-MAPbI₃ mC-PSCs are fabricated with the procedure indicated by the manufacturer while the CsPbI₃:EuCl₃ mC-PSCs are prepared through an optimized recipe.^[27] Both kinds of samples are fabricated in N₂-filled glovebox. The active area of the devices is 144 mm².

Figure 1a shows the X-ray diffraction (XRD) patterns of mC-PSCs infiltrated with CsPbI₃:EuCl₃ or AVA-MAPbI₃. The measurements were performed in N₂ environment in a dome-covered stage to avoid sample degradation after preparation. The common peak in the two patterns located at $2\theta = 26.5^\circ$ is the graphite-based electrode contribution. The AVA-MAPbI₃ sample shows the characteristic prominent peaks of the tetragonal phase at $2\theta = 13.97^\circ$, $2\theta = 14.13^\circ$, $2\theta = 23.52^\circ$, and $2\theta = 24.51^\circ$ related to (002), (110), (211), and (202) planes, respectively. Residual lead iodide (PbI₂) with a characteristic peak at $2\theta = 12.67^\circ$ was not found in the pattern. The CsPbI₃:EuCl₃ pattern is instead characterized by peaks of the photo-active orthorhombic γ -phase, with main contributions at $2\theta = 14.3^\circ$ and $2\theta = 28.9^\circ$ (28.4° in AVA-MAPbI₃). Contributions from the yellow orthorhombic δ -phase (diagnostic peak at $2\theta = 9.8^\circ$) are not found, confirming the purity and the quality of the fabricated perovskite layer. We previously reported the presence of residual yellow orthorhombic δ -phase in CsPbI₃:EuCl₃ infiltrated into mC-PSCs with preparation outside the glovebox,^[27] meaning that the preparation procedure in N₂-filled glovebox could be preferred from the side of the layer purity.

Figure 1b displays the absorption coefficient of AVA-MAPbI₃ and CsPbI₃:EuCl₃ films measured by Spectroscopic Ellipsometry, showing the different bandgap of the materials which is 1.60 and 1.76 eV, respectively.

Figure 1c–d show representative J - V curves for CsPbI₃:EuCl₃ and the reference AVA-MAPbI₃ mC-PSCs measured in forward and reverse scan under solar simulator (AM 1.5, 100 mW cm⁻², scan rate = 50 mV s⁻¹) by varying the illuminated area of the device.

By illuminating an area of 4.2 mm², the AVA-MAPbI₃ mC-PSC achieves a high power conversion efficiency (PCE) of 11.77% in the reverse scan, a value in agreement with other similar small-area devices reported in the literature^[21] with often humidity thermal treatment applied^[25,26] It has an open-circuit voltage (V_{OC}) of 0.8 V, a FF of 73.4% and a short-circuit current density (J_{SC}) of 19.8 mA cm⁻². The efficiency value in the forward scan is equal to 5.06% notably lower than the value in the reverse scan due to a huge hysteresis (Hysteresis index^[31] (HI) = 57%). This phenomenon is well-known for this kind of devices^[26] and it is attributed to the migration of mobile ions into the MAPbI₃ layer.^[32] An additional role in ions migration is played by the c-TiO₂ layer^[33] in the device architecture. The hysteresis phenomenon will be further discussed hereinafter. In contrast, CsPbI₃:EuCl₃ mC-PSC shows a J_{SC} of 14.98 mA cm⁻², a V_{OC} of 1.01 V and an FF of 62.2% resulting in a reverse scan efficiency of 9.41%. The efficiency value is higher than what previously reported for small-area CsPbI₃:EuCl₃ mC-PSC but fabricated outside the glovebox (5.2%),^[27] in agreement with the XRD data showing a better perovskite film quality in the first case. A first observation is thus that the hysteresis phenomenon can be reduced by infiltrating a perovskite with CsPbI₃:EuCl₃ compared to what was achieved using AVA-MAPbI₃, being the HI value reduced from 57% to 14.7%.

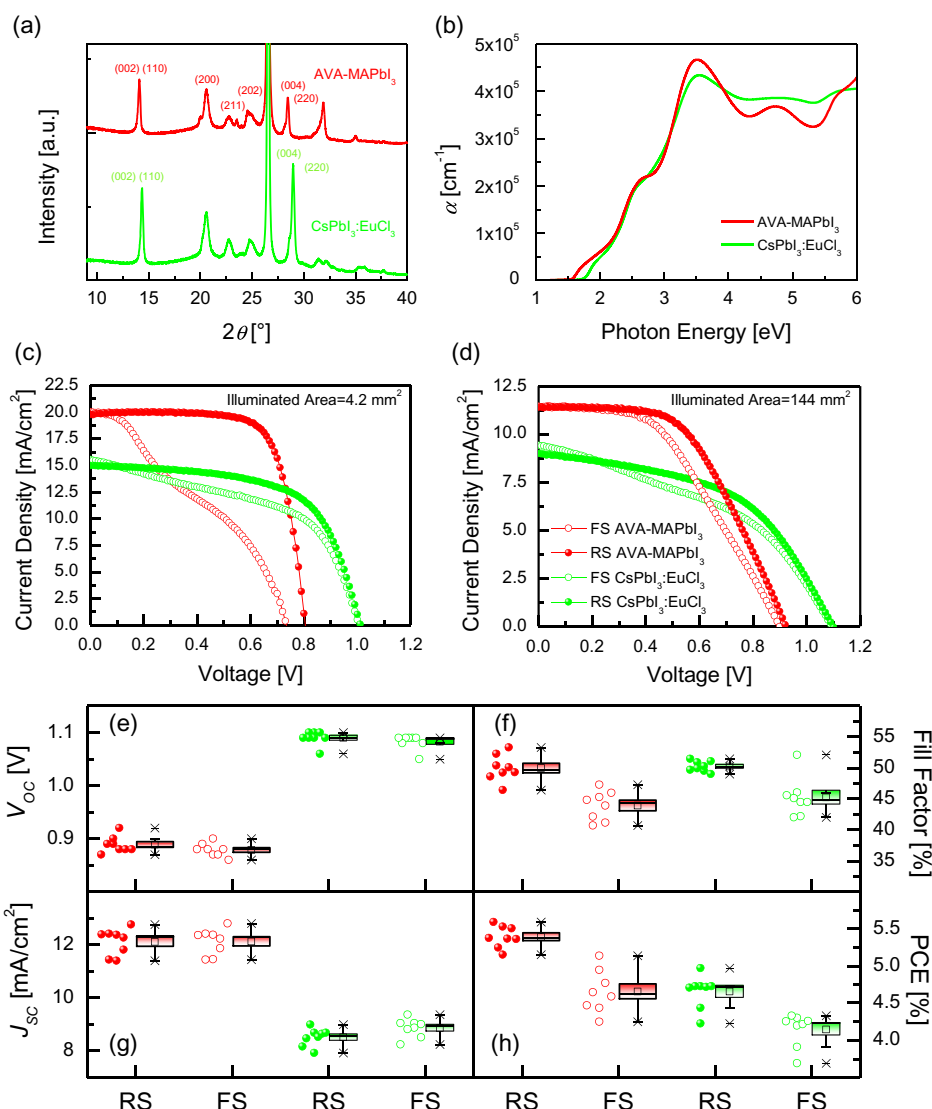


Figure 1. a) X-ray diffraction (XRD) patterns for mC-PSCs infiltrated with AVA-MAPbI₃ and CsPbI₃:EuCl₃. b) Absorption coefficient extracted from spectroscopic ellipsometry measurements in AVA-MAPbI₃ and CsPbI₃:EuCl₃ films. Representative *J*-*V* curves for AVA-MAPbI₃ and CsPbI₃:EuCl₃ mC-PSCs measured in forward (FS) and reverse (RS) scan under solar simulator (AM 1.5, 100 mW cm⁻², scan rate = 50 mV s⁻¹) for c) 4.2 mm² and d) 144 mm² illuminated area. Statistical data of photovoltaic (PV) parameters (e) *V*_{OC}, f) FF, g) *J*_{SC}, and h) PCE related to eight mC-PSCs (illuminated area = 144 mm²) infiltrated with AVA-MAPbI₃ and CsPbI₃:EuCl₃. Red data: AVA-MAPbI₃; green data: CsPbI₃:EuCl₃; filled symbols: RS; empty symbols: FS.

By illuminating the full area of the device (144 mm²), the *V*_{OC} of both kinds of devices increase (0.92 V for AVA-MAPbI₃ and 1.1 V CsPbI₃:EuCl₃), while *J*_{SC} and FF decrease (Table S1, Supporting Information), resulting in efficiency values of 5.59% (no bump) and 4.97% for AVA-MAPbI₃ and CsPbI₃:EuCl₃, respectively. In addition, the hysteresis in large-area mc-PSCs reduces with respect to small-area devices, with HI value of 12.8% for CsPbI₃:EuCl₃ and 15.3% for AVA-MAPbI₃. The huge jump in HI, measured on AVA-MAPbI₃ devices and not observed in CsPbI₃:EuCl₃, which starts denoting a size-dependent behavior of the ionic component kinetics under an electric field. The reported large-area efficiency value for AVA-MAPbI₃ mC-PSC is similar to those already reported in the literature for the same device architecture. In ref. [22], devices with

150 mm² area exhibited efficiency of 7.35% (scan rate 4 mV s⁻¹, bump included (or 6.3% estimated by excluding the bump) to be compared with 144 mm² area shown in this work with efficiency 5.59% (without bump). By performing long-lasting humidity thermal treatments higher efficiencies can be achieved (10% estimated by excluding the bump, on 150 mm² area devices).^[22] In ref. [34] manual drop casting processes are applied, and 5.63% efficiency is generated in 50 mm² area devices (scan rate 20 mV s⁻¹, no bump). The lower efficiency value for the large-area compared to small-area devices is likely due to the limited conductivity of the carbon electrode (see the slope of the *J*-*V* curve at the *V*_{OC} in Figure 1c,d), resulting in lower FF, and to the non-uniform infiltration^[35] of the perovskite by manual drop-casting method which lowers the *J*_{SC}. For this reason, better

performances can be achieved by infiltrating perovskite through automatic semi-continuous dispensing processes^[19,24] or inkjet method.^[36,37] As a matter of fact, ref. [22], in addition to drop casting, reports on inkjet procedure applied to large area devices (150 mm²) and shows a PCE of 7.3% with AVA-MAPbI₃ (no bump without humidity thermal treatment). Hereinafter, we discuss the behavior of large area devices (144 mm²) produced by manual drop-casting and without humidity thermal treatment for comparative analyses of average properties.

Figure 1e–h show the statistical data of PV parameters (V_{OC} , FF, J_{SC} , and PCE) related to eight different mC-PSCs devices infiltrated with CsPbI₃:EuCl₃ in comparison with reference devices infiltrated with AVA-MAPbI₃ (illuminated area = 144 mm²).

CsPbI₃:EuCl₃ mC-PSC shows a lower average value of J_{SC} (8.5 mA cm⁻²) compared to AVA-MAPbI₃ (12.1 mA cm⁻²) but a higher average value of V_{OC} (1.09 V vs 0.89 V), as expected due to the higher bandgap of the perovskite (1.76 eV vs

1.6 eV), and a similar FF ($\approx 50\%$) resulting in an average reverse scan efficiency of 4.7% (5.4% for the AVA-MAPbI₃ device).

To further investigate the hysteresis phenomenon in mC-PSCs, we performed J - V measurements at a lower scan rate, specifically at 6 mV s⁻¹, similar to the value used in the literature for the same device architecture (4 mV s⁻¹).^[22,26] Figure 2a compares the J - V curves of AVA-MAPbI₃ mC-PSC acquired on the same device, firstly biased at the step of 50 mV s⁻¹ and after at the step of 6 mV s⁻¹. All the PV parameters change by varying the scan rate, as shown in Table 1. It is noteworthy that by reducing the scan rate, the HI AVA-MAPbI₃ mC-PSC increases from 18.7% to 41.3% and a bump appears in the reverse scan, causing an inflation in the FF value and PCE values. Such a bump was previously reported in other works where a low scan rate was used for the measurements (4 mV s⁻¹).^[22] On the contrary, the J - V curves of CsPbI₃:EuCl₃ mC-PSCs (Figure 2b) are not as sensitive as AVA-MAPbI₃ mC-PSCs to the change in the scan

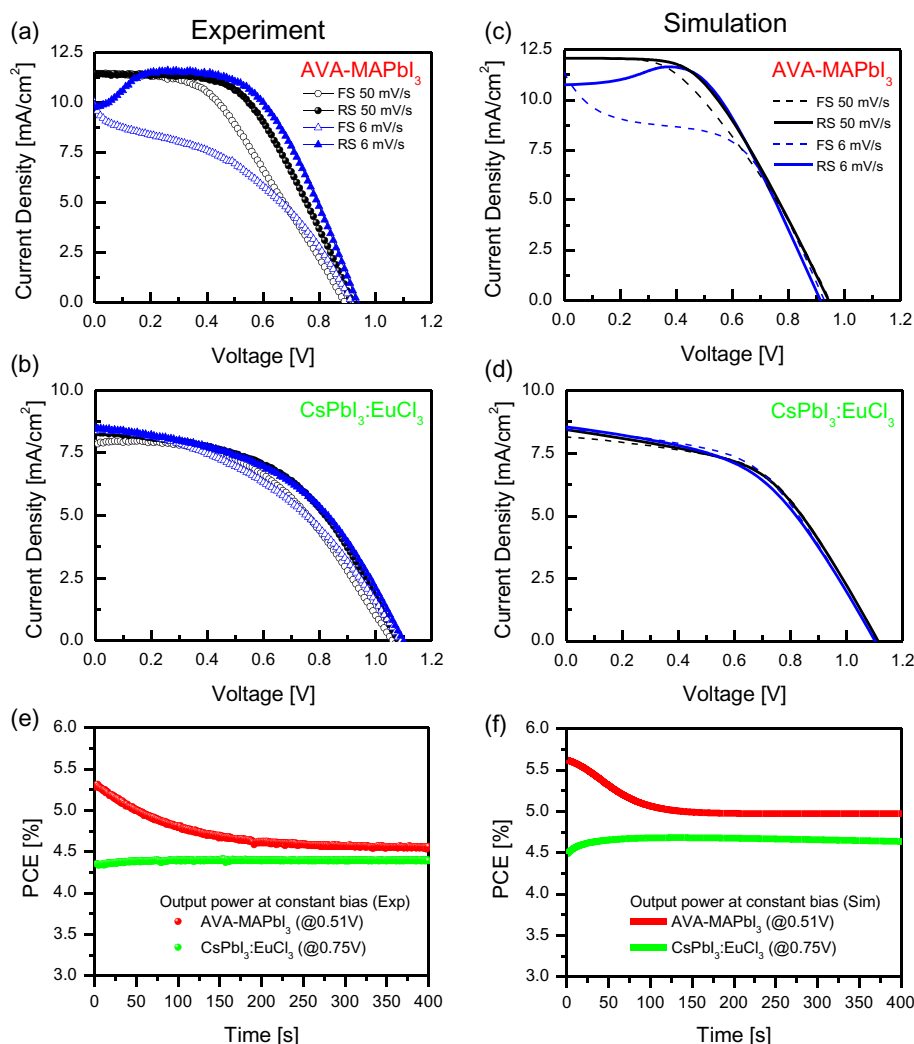


Figure 2. Experimental J - V curves of AVA-MAPbI₃ a) and CsPbI₃:EuCl₃ b) mC-PSC acquired at 50 mV s⁻¹ and at 6 mV s⁻¹. Simulated J - V curves of AVA-MAPbI₃ c) and CsPbI₃:EuCl₃ d) mC-PSC acquired at 50 and at 6 mV s⁻¹. Experimental e) and simulated f) steady-state efficiencies of AVA-MAPbI₃ and CsPbI₃:EuCl₃ mC-PSC measured at constant bias voltages of 0.51 and 0.75 V (voltages of the maximum power point), respectively.

Table 1. Photovoltaic parameters values extracted from representative J - V curves for AVA-MAPbI₃ and CsPbI₃:EuCl₃ mC-PSCs measured in forward and reverse scan for different scan rate (50 and 6 mV s⁻¹). Active area 144 mm².

	Scan rate [mV s ⁻¹]	V _{oc} [V]		FF [%]		J _{sc} [mA cm ⁻²]		PCE [%]		HI [%]
		FS	RS	FS	RS	FS	RS	FS	RS	
AVA-MAPbI ₃	50	0.89	0.92	43.9	52.3	11.43	11.44	4.47	5.50	18.7
	6	0.92	0.94	39.0	65.6	9.81	9.73	3.52	6.00	41.3
CsPbI ₃ :EuCl ₃	50	1.06	1.08	48	49.7	7.91	8.33	4.03	4.47	9.8
	6	1.09	1.1	42.6	47.3	8.36	8.51	3.89	4.43	12.2

rate, with close hysteresis indexes at the two scan rates (9.8% at 50 mV s⁻¹ and 12.2% at 6 mV s⁻¹).

Understanding the origin of such a different hysteretic behavior in CsPbI₃:EuCl₃ mC-PSCs vs. AVA-MAPbI₃ mC-PSCs is not trivial and demands to a deeper investigation. AVA-MAPbI₃ mC-PSCs are used as reference since already widely investigated in literature. It is indeed well known that, whatever the PSCs architecture, the phenomenon of electrical hysteresis is the result of a complex interplay between the ionic response and the electronic response in the perovskite. In turn, these may be affected by perovskite quality, composition of transporting materials, voltage pre-biasing, carrier recombination and, especially, by ionic species mobilities and concentrations. In a transient electrical measurement, both cations and anions in the perovskite diffuse toward the transporting layers, modifying the built-in electric field and hence the carrier distribution into the device, to a different extent depending on the bias history.^[31] It is generally accepted that the mobile species in halide perovskites can either be halide,^[38–42] organic,^[43,44] or metal electrode ions,^[45,46] with the latter being absent in mC-PSCs due to the lack of metal contacts and the organic ions migration (such as MA⁺) occurring at timescales of hours.^[44] It was also reported that hysteresis does not occur when the scan rate is much higher or much lower than the system response rate.^[47] In the first case the mobile ions cannot react to the bias applied and their effect at the interface is weak causing no significant modifications in the built-in electric field; in the second case the mobile ions have sufficient time to accumulate at the interface, reaching their equilibrium distribution at every voltage point and hence making the forward and reverse scans similar. In the case of AVA-MAPbI₃ mC-PSC, we find that both scan rates induce hysteresis. Yet, the increase in HI obtained by lowering the rate to 6 mV s⁻¹ is the evidence that the ionic displacement and accumulation at the interfaces are more strongly affected by the bias history. In addition to this, we also checked that further lowering the scan rate to 1 mV s⁻¹ restores the low HI (see Figure S1, Supporting Information). This suggests that the timescale of the response for this kind of perovskite could be probed by scanning at 6 mV s⁻¹. On the contrary, our results for CsPbI₃:EuCl₃ suggest that both 6 and 50 mV s⁻¹ scan rates are somewhat far from the system response rate. We argue that these differences in HI and scan rate dependence can be attributed to a lower mobility of cations (presumably I⁻ vacancies) in CsPbI₃:EuCl₃ mC-PSCs. Indeed, there is a consensus that I⁻ vacancies (cations) are the most mobile species in halide perovskites^[38,39,40,41] and that large Cs⁺ ions (cations) hinder the migration of I⁻ vacancies.^[48,49]

To corroborate this hypothesis, we have performed 1D transient-mode electro-optical simulations of the two fabricated mC-PSCs (matching layer thicknesses, incident spectrum, and illuminated area) while including the effect of both anion and cation migration within the active regions of the stacks (i.e., mp-TiO₂ and mp-ZrO₂ incorporating the perovskites). We note that cations (anions) in the simulations are defined as generic mobile positive (negative) charges. These are based on the complete formalism implemented in the Setfos software by Fluxim.^[50] The schematic of the device and the band alignments used in the simulations are shown in Figure S2 of the Supporting Information. The charge generation profile in the active layers is calculated with the transfer-matrix method calibrated with the wavelength-dependent complex refractive indices of all layers. These were extracted from ellipsometry measurements available in the literature and are reported in Figure S3 (Supporting Information). This photoconversion model is self-consistently coupled with a drift-diffusion charge transport solver which accounts for charge trapping, recombination and ion migration. All the layer-specific electrical parameters were calibrated to reproduce the main features of the measured J - V curves, based on reasonable initial values reported in the literature (see Table S2, Supporting Information). The mp-TiO₂ and mp-ZrO₂ layers infiltrated with perovskite were modelled in such a 1D electro-optical simulator by following the state-of-the-art approach by Kerremans et al.^[51] i.e., the Bruggeman's Effective Medium Approximation^[52] (EMA) is used to define the optical constants of the two mixed oxide-perovskite layers, assuming 100% pores filling, with electronic parameters (i.e., band edges, effective density of states, carrier mobilities, traps density, and recombination rates) defined as those of the bulk perovskite (see again Table S2, Supporting Information). We note that such a blend-like description, unavoidable in a 1D model, neglects the complex 3D morphology of the mesoporous oxides, where extended perovskite-oxide interfaces exist and are likely to cause local ionic charge accumulation.^[53] Furthermore, it also neglects spatial inhomogeneities due to non-ideal infiltration, as well as possible electronic structure alterations induced by the perovskite confinement in the nanometric pores.^[54,55] Further details about the model, its limitations and the optimized set of parameters can be found in the Supporting Information.

Figure 2c,d show the simulated J - V curves at 50 and 6 mV s⁻¹ for AVA-MAPbI₃ and CsPbI₃:EuCl₃ mC-PSCs, respectively. The main features found in Figure 2a,b are well reproduced by the simulations: the simulated J_{sc} and V_{oc} match those of the measured ones within the experimental uncertainties (see Figure 1e–h)

and the observed deviations are in line with those reported in most state-of-the-art optoelectronic PSCs simulation studies including ion migration.^[50,56–58] Therefore, they can be regarded as a sufficiently reliable basis for getting deeper insights on the different hysteretic behavior of the two mC-PSCs. By comparing the two sets of fitting parameters used to simulate the AVA-MAPbI₃ and CsPbI₃:EuCl₃ mC-PSCs (see Table S2, Supporting Information) we find, as expected, that the most significant difference lies in the cation mobilities, that is $2 \cdot 10^{-11} \text{ cm}^2 \text{ Vs}^{-1}$ for AVA-MAPbI₃ and $3.7 \cdot 10^{-14} \text{ cm}^2 \text{ Vs}^{-1}$ for CsPbI₃:EuCl₃. This large difference ensures good agreement with experiments (in particular the small hysteresis and negligible scan rate dependence of CsPbI₃:EuCl₃) despite the 4–5 times higher cation concentration in CsPbI₃:EuCl₃ obtained from the fit (see Table S2, Supporting Information), which would tend to increase its hysteresis. We also find that the anion mobility in both perovskites is much lower than the cation mobility, in agreement with the literature.^[48,49,50,51] It was reported that, in such cases, including both species or just cations as mobile species in simulations yields identical electrical results.^[50] It is worth mentioning that charge trapping and recombination were also modelled in the simulations by setting the same parameters for the two perovskites (see Table S2, Supporting Information). We find that they only cause a minor variation of J_{SC} , without affecting the overall shape of the J – V curves (see Figure S4, Supporting Information).

We note that the value of the fitted cation mobility for AVA-MAPbI₃ is roughly one order of magnitude smaller than the lowest limit typically reported for bulk organic lead halide perovskites.^[50,59,60] The fitted cation mobility for CsPbI₃:EuCl₃ is also smaller than typical reported values for inorganic lead halide perovskites.^[61] This could be attributed to an effective description of the mesoporous nature of the embedding oxides. It was indeed suggested that the constrained perovskite grains size inside the pores and the related increase in density of grain boundaries partially hinders ion migration.^[53] The non-ideal infiltration of the perovskite by drop-casting could also explain the discrepancy, besides justifying the low photon-to-charge conversion efficiency in the mixed active layers ($\approx 54\%$ for AVA-MAPbI₃ and $\approx 34\%$ for CsPbI₃:EuCl₃) obtained from the fit (see Table S2, Supporting Information). Replacing the EMA with a more sophisticated model of the mixed perovskite/oxide layers, and carrying out a comprehensive fitting procedure based on multiple experimental techniques,^[31] including a statistics to reflect the unavoidable experimental uncertainties, would certainly deliver more accurate estimations of the ionic mobilities. However, for the purposes of this work, the significant difference in cation mobility between the two perovskites already provides a strong indication that it is a major reason behind their different hysteretic behavior.

The different hysteretic behavior and the peculiar “bumped” shape of the AVA-MAPbI₃ RS curve at 6 mV s^{-1} can be framed in terms of carrier and ionic distributions within the mp-TiO₂ and mp-ZrO₂ regions infiltrated with the perovskites. This is clear from **Figure 3**, where we plot the simulated carrier and ionic densities in the active layers at three instants during FS and RS (corresponding to short-circuit, maximum power point, and open circuit conditions) at a 6 mV s^{-1} for the two materials. The ionic contribution within the perovskite/oxide EMA layers comes from the perovskite. For convenience, given the very

low anion mobilities derived from the fitting, here the anion density was modelled as a homogeneously distributed fixed charge. **Figure 3a** shows that the mp-TiO₂ + AVA-MAPbI₃ region close to the electron-transporting c-TiO₂ layer changes its net polarity from negative to positive (positive to negative) during the forward (reverse) voltage scan, due to cations’ migration. This is because the built-in potential tends to move positive charges toward the electron-transporting layer (ETL) in FS and away from it in RS. As shown in **Figure 3b**, such a change of polarity does not occur for CsPbI₃:EuCl₃, due to a much less pronounced cation displacement. The electrons and holes densities across the device reflect the different ionic behavior. Indeed, the profiles at equivalent voltages during FS and RS are quite different in the case of AVA-MAPbI₃, whereas they do not differ as much in the case of CsPbI₃:EuCl₃. This has a direct impact on the FS and RS J – V curves and confirms the lower hysteresis index in the CsPbI₃:EuCl₃ case can be attributed to a suppressed cation migration. The same arguments apply to both mC-PSCs when scanning at 50 mV s^{-1} scan rate, which is too fast even for the cations in the AVA-MAPbI₃. We also note that, at the interface with carbon, the voltage-induced cation density variation is negligible with respect to the overall cation density therein, which we find to be higher than at the c-TiO₂ interface by ≈ 2 orders of magnitude. From a deeper analysis of **Figure 3a** it also becomes clear that the “bump” observed in the experimental and simulated RS curves at 6 mV s^{-1} for AVA-MAPbI₃ is due to the aforementioned change in polarity. This can be proven by contradiction, by simulating a situation where cations are “frozen” at their equilibrium distribution at V_{MPP} during the whole voltage scan. As shown in **Figure S5** (Supporting Information), in this hypothetical case the electron density would manage to overcome the hole density in proximity of the interface with c-TiO₂, thus preventing the current drop observed between V_{MPP} and $V = 0$ in the RS.

It is well known that ion migration is a key factor in the PSCs performance stability,^[62] also due to further reactions occurring at the interfaces with the charges transporting layer and the electrodes. **Figure 2e** displays steady-state efficiencies of AVA-MAPbI₃ and CsPbI₃:EuCl₃ mC-PSC measured at a constant bias voltage of 0.51 and 0.75 V (voltages of the maximum power point), respectively. The CsPbI₃:EuCl₃ mC-PSC exhibits an almost constant efficiency of 4.4% since $t = 0 \text{ s}$, with only a slight noticeable increase within the first 50–100 s, while the AVA-MAPbI₃ mC-PSC shows a slow decay from 5.3% to 4.53% in $\approx 300 \text{ s}$. We argue that the latter decay in the efficiency of the AVA-MAPbI₃ mC-PSC is strictly connected to the hysteresis effect previously shown in J – V curves, with the ionic migration having a pivotal role. This is indeed confirmed by the transient simulations, whose results are shown in **Figure 2f**. These are based on the previously optimized model, but now, with an initial bias preconditioning at open-circuit condition, a constant bias voltage is maintained for 400 s, namely 0.51 V for AVA-MAPbI₃ and 0.75 V for the CsPbI₃:EuCl₃. **Figure S6** (Supporting Information) shows that the descending trend of the AVA-MAPbI₃ mC-PSC is due to the cation displacement (depletion) occurring at the c-TiO₂ interface which affects strongly the electrons and holes distributions. In the CsPbI₃:EuCl₃ mC-PSC the cations are much slower and therefore electrons and holes redistributions are limited by cation displacement (accumulation) occurring in the bulk mp-TiO₂ region.

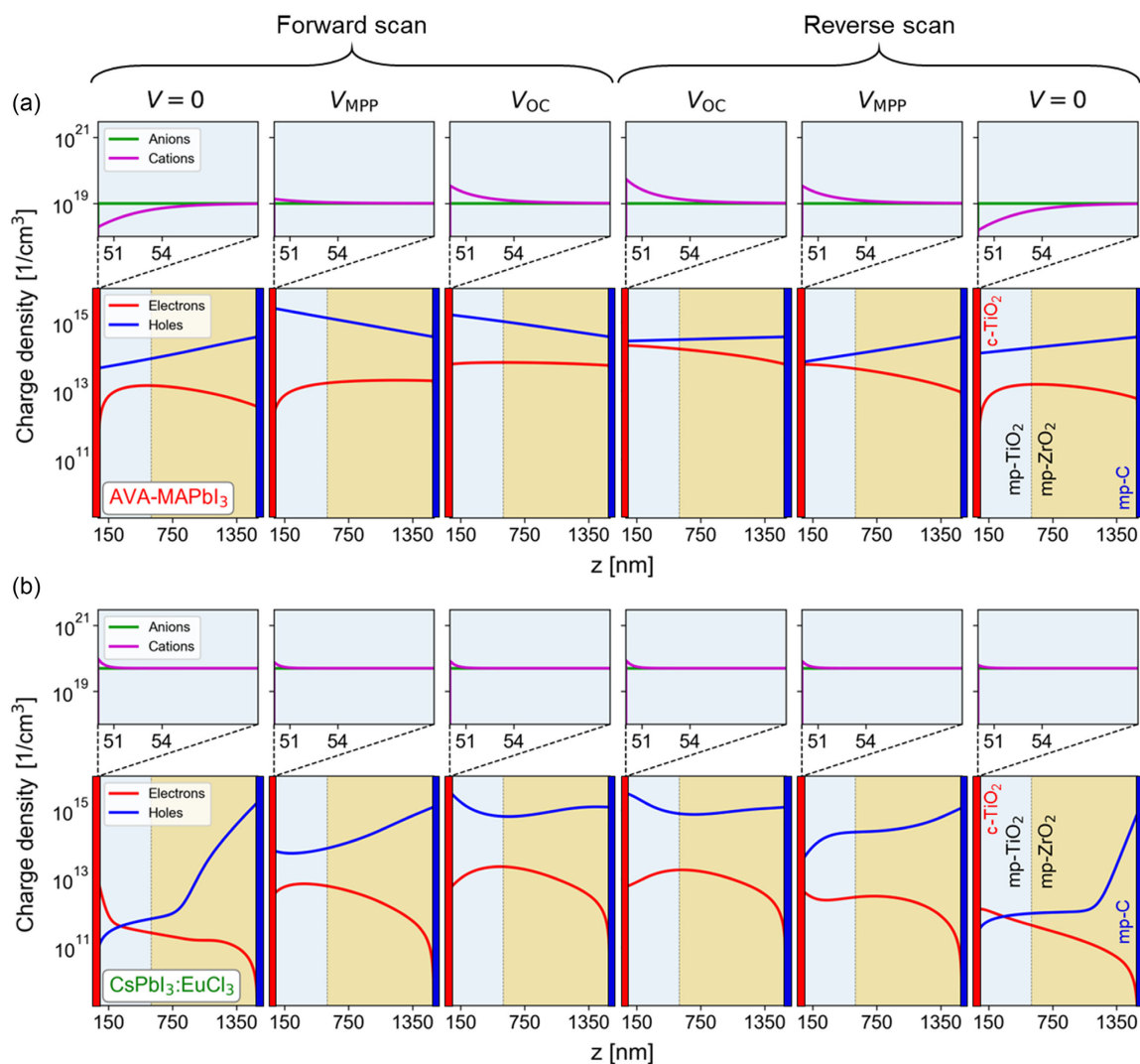


Figure 3. Simulated charge distribution in the mp-TiO₂ and mp-ZrO₂ regions of the mC-PSCs with infiltrated a) AVA-MAPbI₃ and b) CsPbI₃:EuCl₃. Panels from left to right show the transient charge distributions at three representative moments in time ($V = 0$, V_{MPP} , and V_{OC}) during subsequent forward and reverse scans (from -0.1 to 1.2 V and vice versa) at a 6 mV s⁻¹ scan rate. For every snapshot, a zoom-in on the ionic distribution within the first 10 nm of mp-TiO₂ is shown. The ETL (c-TiO₂) and HTL (mp-C) are indicated in all panels with red and blue boxes, respectively.

The latter slightly favors electron accumulation in the proximity of the c-TiO₂ and thus causes a tiny increase in current over time.

In short, despite CsPbI₃:EuCl₃ mC-PSC efficiency is lower at the beginning compared to AVA-MAPbI₃ mC-PSC, its steady-state efficiency is almost the same. CsPbI₃:EuCl₃ mC-PSC long-term stability in N₂ environment under thermal stress (55 °C) and constant illumination through cool-white LED was investigated through maximum power point tracking (MPPT), similarly to what has been done in the literature for AVA-MAPbI₃ mC-PSC.^[23] **Figure 4a** shows that the CsPbI₃:EuCl₃ mC-PSC efficiency is very stable for 250 h, likewise the already reported AVA-MAPbI₃ mC-PSC.^[18,23] This result confirms that the mC-PSC device architecture allows high stability of performances, being both the interfaces between PSK/TiO₂ and PSK/carbon well established. In the case of CsPbI₃:EuCl₃ perovskite, the major degradation factor is the phase transition from the

photoactive black phase to the non-photoactive yellow phase, which is promoted by humidity in ambient air.^[60]

In Ref. [27], we have shown that CsPbI₃:EuCl₃ orthorhombic γ -black phase owns the advantage of phase reversibility. Thus, once the black phase is converted into the yellow phase during ageing, it can be reconverted into the black phase by an annealing process at 350 °C for 2 min that is compatible with the materials in the architecture, thus enabling the reuse of the whole mC-PSC. In contrast, the AVA-MAPbI₃ has an issue with ageing that CsPbI₃ does not have: a mass loss due to volatile species formation as byproducts. This causes irreversible degradation from MAPbI₃ to PbI₂. From the circular economy perspective, Bogachuk et al.^[63] have shown the possibility to recycle the AVA-MAPbI₃ mC-PSCs by washing the carbon and the AVA-MAPbI₃ layer through specific solvents. We have instead focused on a solvent-free reuse process that does not involve additional

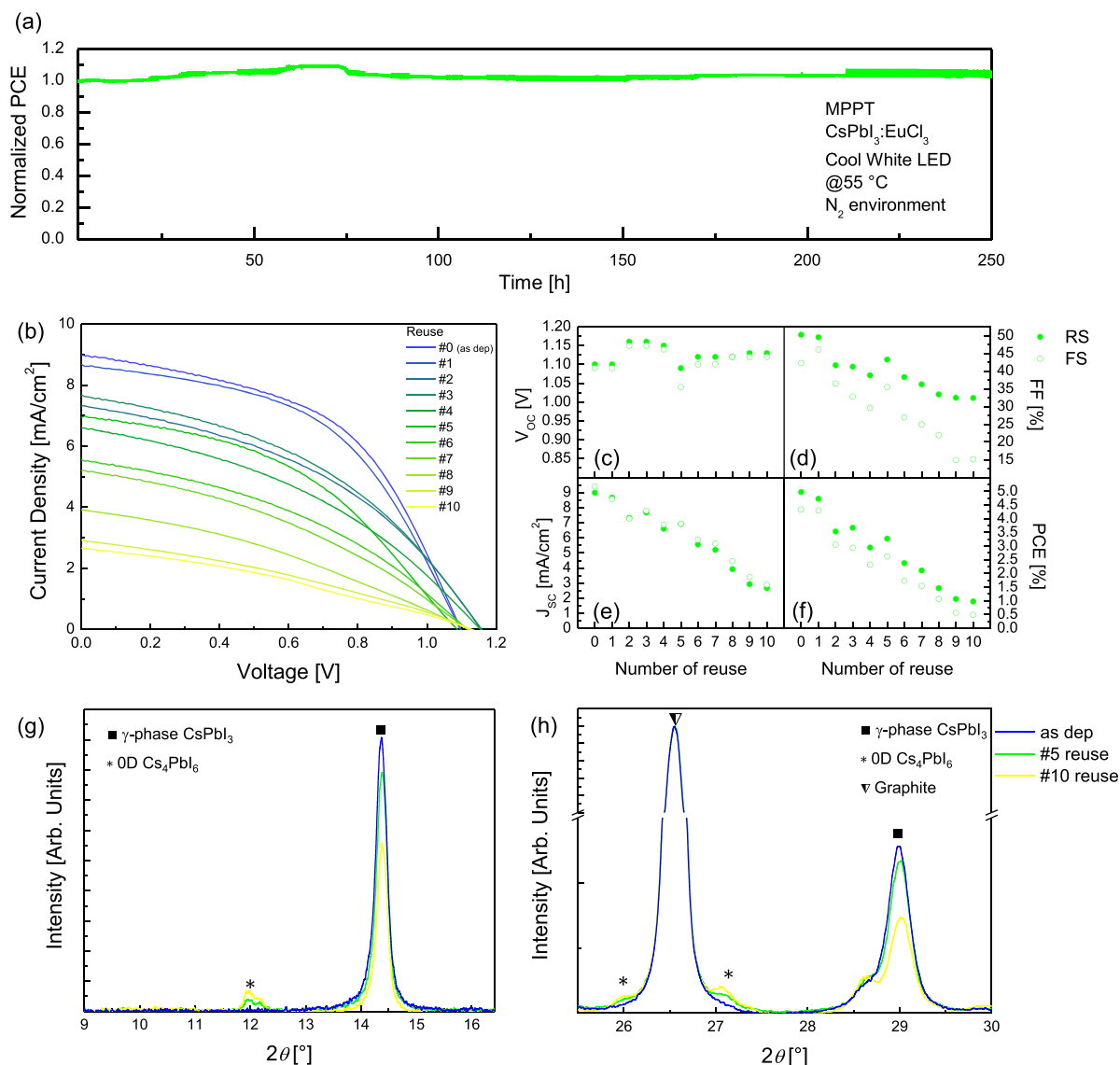


Figure 4. a) 250 h MPP tracking of CsPbI₃:EuCl₃ mC-PSC under thermal stress (55 °C) and constant illumination through cool-white LED in N₂ environment. b) *J*-*V* curves of CsPbI₃:EuCl₃ mC-PSC from 1st to 10th reuse. V_{oc}, c) FF, d) J_{sc}, e) and PCE f) for CsPbI₃:EuCl₃ mC-PSC from 1st to 10th reuse. XRD patterns of CsPbI₃:EuCl₃ mC-PSC acquired for the as prepared mC-PSC and after 5 and 10 reuses in the 2θ range of g) 9°–16.5° and h) 25.5°–30°.

steps except for the annealing. To further go deeper into the reusability of CsPbI₃:EuCl₃ mC-PSC, we have performed 10 reuses on the same mC-PSC device and monitored the photovoltaic parameters. The resulting *J*-*V* curves after every reuse are shown in Figure 4b. We observe that after the first reuse the device is almost unchanged, while after the second reuse, the performance starts decreasing. This is mainly due to a decrease of J_{sc} and fill factor while the V_{oc} slightly increases after several reuses (Figure 4c–f). Overall, a relative decrease of PCE by 34% and 80% after 5 and 10 reuses occurs (Table S3, Supporting Information). To explain this decrease, we performed XRD analyses on mC-PSC after 1, 5, and 10 reuses (Figure 4g,h). They show the progressive decrease of the peaks at 2θ = 14.3° and 2θ = 28.9° related to γ-CsPbI₃ black phase and the formation

of additional peaks at 2θ = 11.9°, 2θ = 25.9, and 2θ = 27.0°. Those peaks grow up along the reuse path and are attributed to 0D Cs₄PbI₆ phase^[64] which is colorless (bandgap = 3.46 eV)^[65] and non-photoactive. We argue that during annealing at 350 °C a progressive sublimation of small amounts of PbI₂ occurs that generates an excess of CsI, inducing Cs₄PbI₆ secondary phase formation at the expense of the CsPbI₃ γ-phase.^[66] It is remarkable to note that the δ-orthorhombic yellow phase was not detected after every reuse, since the diagnostic peak at 2θ = 9.8° is not found. The demonstrated double reuse of the devices with almost unchanged performances would allow doubling the shelf life of the solar module or panels. In addition, focused strategies to avoid the formation of the Cs₄PbI₆ by-product can be implemented to preserve the efficiency of the as-deposited mC-PSC

after every reuse. Reducing the annealing temperature in the recycling protocol would mitigate or even suppress the formation of the secondary phase, and this could be achieved by introducing bromides in the perovskite formulation.^[67] From a sustainability perspective, the superiority of CsPbI₃:EuCl₃ perovskite compared to AVA-MAPbI₃ is given by the possibility of reusing the CsPbI₃ mC-PSC multiple times. Consequently, refurbishing the entire mC-PSC can be proposed as a protocol until a threshold value is reached (e.g., 30% loss). After that, a simple procedure of partial recycling of the architecture can be applied by mechanically removing the carbon electrode and washing the infiltrated perovskite from the mesoporous layers.

3. Conclusion

In summary, we propose a comparative analysis of two perovskite formulations integrated into the same device structure made of layered mesoporous materials and without the HTL/metal component. The use of this device structure avoids the diffusion of metallic species from the top electrode during ageing and, in addition, enables high temperature annealing for sample preparation and eventual reuse. A systematic study, through experiments and simulations, is done by introducing CsPbI₃:EuCl₃ into the device architecture as the main key-study bearing advantages from the presence of a single inorganic cation (Cs).

We assessed the PV performance of CsPbI₃:EuCl₃ infiltrated into mC stack through manual drop-casting, using AVA-MAPbI₃ as a reference. We mainly focused on devices with a total active area of 144 mm². The CsPbI₃:EuCl₃ mC-PSC demonstrated a maximum efficiency of 4.97% with negligible hysteresis (HI = 12.2% at 6 mV s⁻¹) in contrast with the AVA-MAPbI₃ behaviour (maximum efficiency 5.59%, HI = 41.3% at 6 mV s⁻¹). The record value in the literature achieved in large area mC-PSC with AVA-MAPbI₃ (bump excluded, without humidity thermal treatment, semi-automatic drop-casting, and on 150 mm² area) is 6.3%. Increasing the scan rate to 50 mV s⁻¹ levels the large gap in the HI values due to the modified dynamics of mobile cations. Device simulations corroborate the experimental findings, providing a consistent scenario of the reported data and revealing the significant impact of ionic migration on the hysteresis behaviour. Notably, the fitted value of the cation mobility for CsPbI₃:EuCl₃ are three orders of magnitude lower than for AVA-MAPbI₃ (3.7 · 10⁻¹⁴ cm² Vs⁻¹ vs 2 · 10⁻¹¹ cm² Vs⁻¹) which yields the lower hysteresis index at low scan rate. Such simulation-based indirect estimations of the different ionic mobilities in the studied perovskites could be improved with further code development aiming at releasing the effective description of the quasi-1D model, thus providing a more accurate description of the meso-structured PSC geometry. Further experimental investigations combining steady-state, transient time-resolved, and frequency-domain measurements could also be useful to support and assess the theoretical estimations. The maximum power point of CsPbI₃:EuCl₃ mC-PSC remained stable under continuous illumination at 55 °C for 250 h. Moreover, we have shown that the CsPbI₃:EuCl₃ mC-PSC can be refurbished multiple times by annealing at 350 °C, confirming the potential of this material and device architecture for sustainable PV technologies.

Supporting Information

Supporting Information is available from the Wiley Online Library or from the author.

Acknowledgements

S.V. and G.C. contributed equally to this work. The authors acknowledge the project SAMOTHRACE “Sicilian micro and nanotechnology research and innovation centre” funded by PNRR-MUR (ECS_00000022, CUP B63C22000620005). This activity was partially supported by the national project, BEYOND NANO Upgrade (CUP G66J17000350007). The authors acknowledge S. Ferranti (CNR-IMM) for technical assistance.

Conflict of Interest

The authors declare no conflict of interest.

Data Availability Statement

The data that support the findings of this study are available from the corresponding author upon reasonable request.

Keywords

CsPbI₃, MAPbI₃, mesoporous carbon, perovskite solar cells, reusable, stability, sustainability

Received: November 22, 2023

Revised: December 13, 2023

Published online:

- [1] A. K. Jena, A. Kulkarni, T. Miyasaka, *Chem. Rev.* **2019**, *119*, 3036.
- [2] H. Min, D. Y. Lee, J. Kim, M. J. Paik, Y. K. Kim, K. S. Kim, M. G. Kim, T. J. Shin, S. I. Seok, *Nature* **2021**, *598*, 444.
- [3] <https://www.nrel.gov/pv/cell-efficiency.html> (accessed: 16 November 2023).
- [4] E. Aydin, E. Ugur, B. K. Yildirim, T. G. Allen, P. Dally, A. Razzaq, F. Cao, L. Xu, B. Vishal, A. Yazmaciyan, A. A. Said, S. Zhumagali, R. Azmi, M. Babics, A. Fell, C. Xiao, S. De Wolf, *Nature* **2023**, <https://doi.org/10.1038/s41586-023-06667-4>.
- [5] Z. Guo, A. K. Jena, T. Miyasaka, *ACS Energy Lett.* **2023**, *8*, 90.
- [6] S. Valastro, E. Smecca, G. Mannino, C. Bongiorno, G. Fisicaro, S. Goedecker, V. Arena, C. Spampinato, I. Deretzis, S. Dattilo, A. Scamporrino, S. Carroccio, E. Fazio, F. Neri, F. Bisconti, A. Rizzo, C. Spinella, A. La Magna, A. Alberti, *Nat. Sustain.* **2023**, *6*, 974.
- [7] H. Zhang, J.-W. Lee, G. Nasti, R. Handy, A. Abate, M. Grätzel, N.-G. Park, *Nature* **2023**, *617*, 687.
- [8] Y. Rong, Y. Hu, A. Mei, H. Tan, M. I. Saidaminov, S. I. Seok, M. D. McGehee, E. H. Sargent, H. Han, *Science* **2018**, *361*, eaat8235.
- [9] S. L. Hamukwaya, H. Hao, Z. Zhao, J. Dong, T. Zhong, J. Xing, L. Hao, *Coatings* **2022**, *12*, 252.
- [10] H. Xu, *IOP Conf. Ser.: Earth Environ. Sci.* **2020**, *585*, 012027.
- [11] S.-W. Lee, S. Kim, S. Bae, K. Cho, T. Chung, L. E. Mundt, S. Lee, S. Park, H. Park, M. C. Schubert, S. W. Glunz, Y. Ko, Y. Jun, Y. Kang, H.-S. Lee, D. Kim, *Sci. Rep.* **2016**, *6*, 38150.
- [12] E. Smecca, Y. Numata, I. Deretzis, G. Pellegrino, S. Boninelli, T. Miyasaka, A. La Magna, A. Alberti, *Phys. Chem. Chem. Phys.* **2016**, *18*, 13413.

- [13] S. Shao, M. A. Loi, *Adv. Mater. Interfaces* **2020**, *7*, 1901469.
- [14] S. Kim, S. Bae, S.-W. Lee, K. Cho, K. D. Lee, H. Kim, S. Park, G. Kwon, S.-W. Ahn, H.-M. Lee, Y. Kang, H.-S. Lee, D. Kim, *Sci. Rep.* **2017**, *7*, 1200.
- [15] K. Domanski, J. P. Correa-Baena, N. Mine, M. K. Nazeeruddin, A. Abate, M. Saliba, W. Tress, A. Hagfeldt, M. Grätzel, *ACS Nano* **2016**, *10*, 6306.
- [16] A. K. Jena, Y. Numata, M. Ikegami, T. Miyasaka, *J. Mater. Chem. A* **2018**, *6*, 2219.
- [17] D. Bogachuk, S. Zouhair, K. Wojciechowski, B. Yang, V. Babu, L. Wagner, B. Xu, J. Lim, S. Mastroianni, H. Pettersson, A. Hagfeldt, A. Hinsch, *Energy Environ. Sci.* **2020**, *13*, 3880.
- [18] M. Hadadian, J. Smätt, J. P. Correa-Baena, *Energy Environ. Sci.* **2020**, *13*, 1377.
- [19] G. Grancini, C. Roldán-Carmona, I. Zimmermann, E. Mosconi, X. Lee, D. Martineau, S. Narbey, F. Oswald, F. De Angelis, M. Graetzel, M. K. Nazeeruddin, *Nat. Commun.* **2017**, *8*, 15684.
- [20] A. Mei, X. Li, L. Liu, Z. Ku, T. Liu, Y. Rong, M. Xu, M. Hu, J. Chen, Y. Yang, M. Grätzel, H. Han, *Science* **2014**, *345*, 295.
- [21] S. M. P. Meroni, C. Worsley, D. Raptis, T. M. Watson, *Energies* **2021**, *14*, 386.
- [22] E. Planes, C. Farha, G. De Moor, S. Narbey, L. Perrin, L. Flandin, *Sol. RRL* **2023**, *7*, 2300492.
- [23] A. Mei, Y. Sheng, Y. Ming, Y. Hu, Y. Rong, W. Zhang, S. Luo, G. Na, C. Tian, X. Hou, Y. Xiong, Z. Zhang, S. Liu, S. Uchida, T.-W. Kim, Y. Yuan, L. Zhang, Y. Zhou, H. Han, *Joule* **2020**, *4*, 2646.
- [24] D. Bogachuk, K. Sadeddine, D. Martineau, S. Narbey, A. Verma, P. Gebhardt, J. P. Herterich, N. Glissmann, S. Zouhair, J. Markert, I. E. Gould, M. D. McGehee, U. Würfel, A. Hinsch, L. Wagner, *Sol. RRL* **2022**, *6*, 2100527.
- [25] S. G. Hashmi, D. Martineau, M. I. Dar, T. T. T. Myllymäki, T. Sarikka, V. Ulla, S. M. Zakeeruddin, M. Grätzel, *J. Mater. Chem. A* **2017**, *5*, 12060.
- [26] S. Zouhair, B. Luo, D. Bogachuk, D. Martineau, L. Wagner, A. Chahboun, S. W. Glunz, A. Hinsch, *Sol. RRL* **2022**, *6*, 2100745.
- [27] S. Valastro, E. Smecca, C. Bongiorno, C. Spampinato, G. Mannino, S. Biagi, I. Deretzis, F. Giannazzo, A. K. Jena, T. Miyasaka, A. La Magna, A. Alberti, *Sol. RRL* **2022**, *6*, 2200267.
- [28] I. Deretzis, C. Bongiorno, G. Mannino, E. Smecca, S. Sanzaro, S. Valastro, G. Fiscaro, A. La Magna, A. Alberti, *Nanomaterials* **2021**, *11*, 1282.
- [29] S. Valastro, G. Mannino, E. Smecca, C. Bongiorno, S. Sanzaro, I. Deretzis, A. La Magna, A. K. Jena, T. Miyasaka, A. Alberti, *Sol. RRL* **2022**, *6*, 2200008.
- [30] S. Valastro, G. Mannino, E. Smecca, S. Sanzaro, I. Deretzis, A. L. Magna, A. K. Jena, T. Miyasaka, A. Alberti, *J. Phys. Mater.* **2021**, *4*, 034011.
- [31] S. N. Habisreutinger, N. K. Noel, H. J. Snaithe, *ACS Energy Lett.* **2018**, *3*, 2472.
- [32] W. Tress, N. Marinova, T. Moehl, S. M. Zakeeruddin, M. K. Nazeeruddin, M. Grätzel, *Energy Environ. Sci.* **2015**, *8*, 995.
- [33] Y. Rong, Y. Hu, S. Ravishanker, H. Liu, X. Hou, Y. Sheng, A. Mei, Q. Wang, D. Li, M. Xu, J. Bisquert, H. Han, *Energy Environ. Sci.* **2017**, *10*, 2383.
- [34] F. De Rossi, J. Barbé, D. M. Tanenbaum, L. Cinà, L. A. Castriotta, V. Stoichkov, Z. Wei, W. C. Tsoi, J. Kettle, A. Sadula, J. Chircop, A. Azzopardi, H. Xie, A. Di Carlo, M. Lira-Cantú, E. A. Katz, T. M. Watson, F. Brunetti, *Energy Technol.* **2020**, *8*, 2000134.
- [35] H. Lakhiani, T. Dunlop, F. De Rossi, S. Dimitrov, R. Kerremans, C. Charbonneau, T. Watson, J. Barbé, W. C. Tsoi, *Adv. Funct. Mater.* **2019**, *29*, 1900885.
- [36] C. M. T. Kim, M. A. N. Perera, M. Katz, D. Martineau, S. G. Hashmi, *Adv. Eng. Mater.* **2022**, *24*, 2200747.
- [37] L. Perrin, L. Flandin, C. Farha, S. Narbey, D. Martineau, E. Planès, *Energies* **2023**, *16*, 5254.
- [38] J. M. Azpiroz, E. Mosconi, J. Bisquert, F. De Angelis, *Energy Environ. Sci.* **2015**, *8*, 2118.
- [39] J. Haruyama, K. Sodeyama, L. Han, Y. Tateyama, *J. Am. Chem. Soc.* **2015**, *137*, 10048.
- [40] M. T. Neukom, A. Schiller, S. Züfle, E. Knapp, J. Ávila, D. Pérez-Del-Rey, C. Dreessen, K. P. S. Zanon, M. Sessolo, H. J. Bolink, B. Ruhstaller, *ACS Appl. Mater. Interfaces* **2019**, *11*, 23320.
- [41] N. E. Courtier, J. M. Cave, J. M. Foster, A. B. Walker, G. Richardson, *Energy Environ. Sci.* **2019**, *12*, 396.
- [42] C. Eames, J. M. Frost, P. R. F. Barnes, B. C. O'Regan, A. Walsh, M. S. Islam, *Nat. Commun.* **2015**, *6*, 7497.
- [43] K. Domanski, B. Roose, T. Matsui, M. Saliba, S.-H. Turren-Cruz, J.-P. Correa-Baena, C. R. Carmona, G. Richardson, J. M. Foster, F. De Angelis, J. M. Ball, A. Petrozza, N. Mine, M. K. Nazeeruddin, W. Tress, M. Grätzel, U. Steiner, A. Hagfeldt, A. Abate, *Energy Environ. Sci.* **2017**, *10*, 604.
- [44] H. Wang, A. Guerrero, A. Bou, A. M. Al-Mayouf, J. Bisquert, *Energy Environ. Sci.* **2019**, *12*, 2054.
- [45] K. Sakhatskyi, R. A. John, A. Guerrero, S. Tsarev, S. Sabisch, T. Das, G. J. Matt, S. Yakunin, I. Cherniukh, M. Kotyrba, Y. Berezovska, M. I. Bodnarchuk, S. Chakraborty, J. Bisquert, M. V. Kovalenko, *ACS Energy Lett.* **2022**, *7*, 3401.
- [46] R. A. John, Y. Demirağ, Y. Shynkarenko, Y. Berezovska, N. Ohannessian, M. Payvand, P. Zeng, M. I. Bodnarchuk, F. Krumeich, G. Kara, I. Shorubalko, M. V. Nair, G. A. Cooke, T. Lippert, G. Indiveri, M. V. Kovalenko, *Nat. Commun.* **2022**, *13*, 2074.
- [47] J.-Y. Huang, Y.-W. Yang, W.-H. Hsu, E.-W. Chang, M.-H. Chen, Y.-R. Wu, *Sci. Rep.* **2022**, *12*, 7927.
- [48] P. Bhatt, A. Kumar, N. Singh, A. Garg, K. S. Nalwa, A. Tewari, *ACS Appl. Energy Mater.* **2023**, *6*, 6615.
- [49] X. Liu, M. Chen, Y. Zhang, J. Xia, J. Yin, M. Li, K. G. Brooks, R. Hu, X. Gao, Y.-H. Kim, A. Züttel, J. M. Luther, S. Kinge, Y. Feng, M. K. Nazeeruddin, *Chem. Eng. J.* **2022**, *431*, 133713.
- [50] Fluxim AG, Semiconducting Thin Film Optics Simulator (SETFOS); version 5.4; Fluxim AG, Switzerland.
- [51] R. Kerremans, O. J. Sandberg, S. Meroni, T. Watson, A. Armin, P. Meredith, *Sol. RRL* **2020**, *4*, 1900221.
- [52] D. A. G. Bruggeman, *Ann. Phys.* **1935**, *416*, 636.
- [53] D. Bogachuk, B. Yang, B. J. Suo, D. Martineau, A. Verma, S. Narbey, M. Anaya, K. Frohna, T. Doherty, D. Müller, J. P. Herterich, S. Zouhair, A. Hagfeldt, S. D. Stranks, U. Würfel, A. Hinsch, L. Wagner, *Adv. Energy Mater.* **2022**, *12*, 2103128.
- [54] C. Spampinato, P. La Magna, S. Valastro, E. Smecca, V. Arena, C. Bongiorno, G. Mannino, E. Fazio, C. Corsaro, F. Neri, A. Alberti, *Solar* **2023**, *3*, 347.
- [55] J. Shamsi, A. S. Urban, M. Imran, L. De Trizio, L. Manna, *Chem. Rev.* **2019**, *119*, 3296.
- [56] M. T. Neukom, S. Züfle, E. Knapp, M. Makha, R. Hany, B. Ruhstaller, *Sol. Energy Mater. Sol. Cells* **2017**, *169*, 159.
- [57] M. Neukom, S. Züfle, S. Jenatsch, B. Ruhstaller, *Adv. Mater.* **2018**, *19*, 291.
- [58] S. Lammar, R. Escalante, A. J. Riquelme, S. Jenatsch, B. Ruhstaller, G. Oskam, T. Aernouts, J. A. Anta, *J. Mater. Chem. A* **2022**, *10*, 18782.
- [59] S. T. Birkhold, J. T. Precht, R. Giridharagopal, G. E. Eperon, L. Schmidt-Mende, D. S. Ginger, *J. Phys. Chem. C* **2018**, *122*, 12633.
- [60] Z. Lin, Y. Zhang, M. Gao, J. A. Steele, S. Louisia, S. Yu, L. N. Quan, C.-K. Lin, D. T. Limmer, P. Yang, *Matter* **2021**, *4*, 2392.
- [61] T. J. A. M. Smolders, A. B. Walker, M. J. Wolf, *J. Phys. Chem. Lett.* **2021**, *12*, 5169.

- [62] T. Tayagaki, K. Yamamoto, T. N. Murakami, M. Yoshita, *Sol. Energy Mater. Sol. Cells* **2023**, 257, 112387.
- [63] D. Bogachuk, P. van der Windt, L. Wagner, D. Martineau, S. Narbey, A. Verma, J. Lim, S. Zouhair, M. Kohlstädt, A. Hinsch, S. Stranks, U. Würfel, S. Glunz, *Res. Sq.* **2022**, <https://doi.org/10.21203/rs.3.rs-1767937/v1>.
- [64] F. Bai, J. Zhang, Y. Yuan, H. Liu, X. Li, C. Chueh, H. Yan, Z. Zhu, A. K. Jen, *Adv. Mater.* **2019**, 31, 1904735.
- [65] C. Li, S. Zhou, J. Nie, J. Huang, X. Ouyang, Q. Xu, *Nano Lett.* **2021**, 21, 102799.
- [66] J. Satta, A. Casu, D. Chiriu, C. M. Carbonaro, L. Stagi, P. C. Ricci, *Nanomaterials* **2021**, 11, 1823.
- [67] T. Niu, W. Zhu, Y. Zhang, Q. Xue, X. Jiao, Z. Wang, Y.-M. Xie, P. Li, R. Chen, F. Huang, Y. Li, H.-L. Yip, Y. Cao, *Joule* **2021**, 5, 249.